

Title here

Elio Campitelli * and Leandro Díaz

CIMA UBA blablabla

Carolina Vera

⁵ **Corresponding author:* Elio Campitelli, elio.campitelli@cima.fcen.uba.ar

ABSTRACT

Enter the text of your abstract here. This is a sample American Meteorological Society (AMS) \LaTeX template. This document provides authors with instructions on the use of the AMS \LaTeX template. Authors should refer to the file `amspaper.tex` to review the actual \LaTeX code used to create this document. The `template.tex` file should be modified by authors for their own manuscript.

10 *Significance statement.* This is significant because I wrote it.

11 **1. Introduction**

12 yada yada SAM yada yada circulation.. yada yada so important. yada yada many impacts.

13 Fogt et al. (2012) studied the characteristics of the asymmetric structure of the SAM. It computed
14 the zonally anomalous component of mean sea level pressure (MSLP) composites for positive and
15 negative SAM events and created two indices by projecting MSLP fields onto them. However,
16 the use of composites leads to some issues that affect the interpretability of the results. First, they
17 can be dependent on the choice of threshold used to define positive and negative events. Secondly,
18 by discarding data that don't meet the threshold, they don't use all the information available. Due to
19 the relatively short timeframe used, this leads to some composites being composed of as little as 4
20 years. Third, the resulting composites corresponding to each polarity and season are derived from
21 the average of different amounts of fields and from different years. This last issue is particularly
22 important in light of the changing structure of the SAM before and after 1980 (Silvestri and Vera
23 2009). In Fogt et al. (2012), the DJF SAM+ composite uses only 7 years, 5 of which are later than
24 1988, whereas all of the 8 years used for their DJF SAM- composite are from earlier than 1988.

25 **2. Methods**

26 **1) DEFINITION OF INDICES**

27 We defined the Southern Annular Mode (SAM) as the leading EOF of the monthly anomalies of
28 geopotential field at 700 hPa south of 20°S (citation?). The EOF was performed by computing the
29 Singular Value Decomposition of the data matrix consisting in 481 rows and 4176 columns (144
30 points of longitude and 29 points of latitude). The values were weighted by the square root of the

31 cosine of latitude to account for the non-equal area of each gridpoint (Chung and Nigam 1999).
32 This same method was used at the rest of the levels considered in this paper.

33 To separate between the zonally symmetric and asymmetric components of the SAM, we com-
34 puted the zonal mean and anomalies of the full SAM spatial pattern. The results are shown in
35 Figure 1 for 700hPa. The full spatial signal ($\text{EOF}_1(\lambda, \phi)$) is the sum of the zonally asymmetric
36 ($\text{EOF}_1^*(\lambda, \phi)$) and symmetric ($[\text{EOF}_1](\lambda, \phi)$) components. We then compute the “Full”, “Asym-
37 metric” and “Symmetric” indices, by regressing each geopotential field on these patterns (weighting
38 by the cosine of latitude).

39 The three indices are normalised by dividing them by the standard deviation of the “Full” index
40 at each level. This means that comparing the magnitude between indices is meaningful, but it also
41 means that not every index will have unit standard deviation.

42 2) DATA

43 We used monthly geopotential height at 2.5 longitude by 2.5 latitude resolution from ERA5
44 (Hersbach et al. 2020) for the period 1979 to 2018.

45 Monthly temperature NOAA Global Surface Temperature (NOAAGlobalTemp) 5.0 degree lati-
46 tude x 5.0 degree longitude global grid (Vose et al. 2012; Smith et al. 2008). The same analysis
47 was carried out using CRUTEM4 (Osborn and Jones 2014) (not shown).

48 We used monthly precipitation data from CPC Merged Analysis of Precipitation (Xie and Arkin
49 1997) 2.5 degree latitude x 2.5 degree longitude. CPCC: [schneider2015] #FIXME

50 3) SIGNIFICANCE

51 We adjusted p-values for False Detection Rate following Wilks (2016).

3. Results

a. Temporal evolution

Figure 2 shows the resulting Asymmetric and Symmetric time series corresponding to 700 and 50hPa. #FIXME

At first glance the series can be distinguished by their distributions. Whereas the tropospheric indices are approximately normally distributed, the stratospheric indices are more long-tailed; that is, extreme values (both negative and positive) abound. The Asymmetric series have both more variability in the higher frequencies than the Symmetric series.

The stratospheric Symmetric SAM varies strongly with a two-year period, which can be seen using spectral methods (Figure A3) or in the autocorrelation structure (Figure A4). There is a local peak at 2 years in the periodogram of the tropospheric Symmetric SAM also, although it's not statistically significant. In the troposphere the most significant peak of variability is found in the Asymmetric index at around 3.6 months.

From Figure 2 we can see that the Asymmetric and Symmetric time series appear to be correlated. Moreover, looking at the extremes in the stratosphere, the Symmetric series appears to lag the Asymmetric series (see, for example, the positive events on late 1987 marked with a circle). We show these correlations, across all the levels of the reanalysis and for zero and -1 lag (Asymmetric index leading the Symmetric index), in Figure 3.

Zero-lag correlations between the Asymmetric and Symmetric series are relatively constant throughout the troposphere, fluctuating between 0.39 and 0.45. One-month-lag correlations are similarly constant but significantly reduced, hovering around 0.17. In the stratosphere, zero-lag correlations drop to a minimum of 0.21 at 20 hPa and then it increases again monotonically with

74 height up to the uppermost level of the reanalysis. At the same time, one-month-lag correlations
75 increase with height.

76 Figure 4a) shows (zero-lag) cross-correlation across levels for the Full, Symmetric and Asym-
77 metric SAM indices. For the Full SAM (panel a), high values below 100 hPa reflect the vertical
78 (zero-lag) coherency throughout the troposphere. Above 100 hPa correlation between levels falls
79 off more rapidly, indicating less coherent (zero-lag) variability. Still there is a non negligible
80 correlation between the troposphere and the lower-to-middle stratosphere. Examining panels b
81 and c, we see that the Asymmetric and Symmetric SAM share the same high level of coherency
82 in the troposphere but they differ in their stratospheric behaviour. As evidenced by the wider
83 dark red areas near the diagonal in Figure 4b) vs. Figure 4c), stratospheric coherency is stronger
84 for the Asymmetric SAM than the Symmetric SAM. The stratospheric Symmetric SAM seems
85 to connect more strongly to the troposphere than the Asymmetric SAM; this can be seen by the
86 lower correlation values in the top right left of Figure 4b) in comparison with Figure 4c).

87 Figure 5 shows normalised decadal trends for each index for the whole period 1979-2018 along
88 with the 95% confidence interval in shading for the whole year (row a) and separated by trimesters
89 (rows b through e). As documented by #FIXME (e.g. Fogt and Marshall (2020)), there is a
90 statistically significant increase towards more positive SAM (panel a.1), which is XX only in
91 Summer and Autumn (panels b.1 and c.1). We observe these increases mainly in the troposphere,
92 reaching their maximum at at 100 hPa in Summer. By separating the SAM signal in its Asymmetric
93 and Symmetric parts, we can not only see that these trends are almost entirely due to the Symmetric
94 component (columns 2 vs. columns 3), but in some cases the trends become more clear. In Summer,
95 the Asymmetric SAM has a statistically non significant negative trend in the middle troposphere
96 that obscures the signal; as a result, trends computed using only the Symmetric component are
97 more clear (compare the shading region in panel b.1 and b.3). In Autumn, using the Symmetric

98 SAM reveals a statistically significant positive trend in the stratosphere that is not significant using
99 the Full index.

100 We stress that these are only linear trends during the whole period and the absence of a statistically
101 significant signal should not be taken as evidence of no systematic change. In particular, going
102 back to Figure 2, we can see an evident change in the stratospheric Asymmetric component (red
103 line in panel a) between the 90's, when we see a dominance of extreme negative values, and the
104 00's, when we see the inverse. This change is restricted to the Winter months: the linear trend for
105 JJA starting in 1990 for the Asymmetric component at 50hPa is 0.37 ± 0.22 .

106 Figure 6 shows decadal trends for the explained variance of each index. There is no evidence of a
107 significant trend in the stratosphere. In the troposphere, there is a positive trend for the Asymmetric
108 SAM and no significant trend for the Symmetric SAM. This suggests that the SAM has become
109 more asymmetric in the period from 1979 to 2018. The change is slight, though; of the order of
110 1% increased explained variance per decade.

111 *b. Spatial patterns*

112 To understand the spatial patterns associated with both indices, we regressed monthly geopotential
113 anomalies into both indices using multiple regression

114 Figure 7 shows the spatial year-long regression *#FIXME*. Column 1 are regressions using the
115 Full SAM, while columns 2 and 3 are regression coefficients computed in a multiple regression of
116 geopotential height on the Asymmetric and Symmetric indices at the same time. Thus, they are
117 to be interpreted as the patterns associated with each index, controlling for the (linear) effect of the
118 other. (Figure A6 *#FIXME* illustrates the difference between computing two simple regressions
119 and one multiple regression.)

120 In the stratosphere, the spatial pattern associated with the Full SAM is more clearly dominated by
121 a zonally symmetric, monopolar structure (panel a.1) which is, however, not perfectly centered in
122 the south pole. The monopole obtained by multiple regression with the Asymmetric and Symmetric
123 SAM (panel a.3) is much more symmetric and the shift from total symmetry is captured by the
124 regression pattern of the Asymmetric SAM as a wave-1 with maximum anomalies above the
125 Belinghausen Sea on the Western Hemisphere and Davids Sea in the Eastern Hemisphere
126 (panel a.2).

127 In the troposphere, panel b.1 shows the well known zonally symmetrical annular mode *contam-*
128 *inated* with zonal asymmetries in the form of a wave-3. The regression using the Asymmetric and
129 Symmetric SAM indices successfully disentangle both structures. The Asymmetric component
130 gives rise to a cleaner zonal wave (panel b.2) and the Symmetric component is associated with an
131 trully annular mode, almost devoid of zonal asymmetries (panel b.3). note that the wave-3 pattern
132 observed in panel b.2 is rotated by half a wavelength from the average position of the mean wave-3
133 pattern and asociated with Raphael (2004)'s ZW3 index (see Figure 1 from that paper). #FIXME
134 (agregar algo más?)

135 The amplitude of each zonal wave number at each latitude at 50 hPa and 700 hPa is shown
136 in Figure 8, where wave number zero represents the amplitude of the zonal mean. Comparing
137 between rows, this Figure quantifies the relatively clean separation between the zonally symmetric
138 and zonally asymmetric structures, as its evident how the mixture of waves of the Full field (column
139 a) is very similar to the sum of the waves of the Asymmetric and Symmetric field (columns b and c,
140 respectively). Column b of Figure 8 shows that the Asymmetric SAM is overwhelmingly dominated
141 by wave 1 in the stratosphere (panel b.1), while in the troposphere it is composed of zonal waves 3
142 to 1 in decreasing level of importance (panel b.2).

143 To analyse the vertical structure of the geopotential anomalies associated with the asymmetric SAM
144 index, we show a vertical cross section of regressions of mean geopotential height between 65°S
145 and 40°S for the 50 hPa Asymmetric SAM index (panel a) and for the 700 hPa Asymmetric SAM
146 index (panel b) (Figure 9).

147 The geopotential anomalies associated with the stratospheric SAM (panel a) are clearly con-
148 strained to the stratosphere, which underscores the disconnect between the stratospheric and
149 tropospheric symmetric SAM. The vertical structure of this signal tilts about 60° to the West between
150 100 hPa and 1 hPa, suggesting baroclinic processes and poleward transport of heat (this is ok?). Interestingly, the signal in the stratosphere maximises near 10 hPa despite using the 50
151 hPa index for the regression.
152

153 The tropospheric asymmetric SAM has significant signals that extend upwards to the uppermost
154 levels of the reanalysis. In the troposphere, the wave-3 structure is equivalent barotropic with
155 maximum amplitude at roughly 250 hPa. This is moaaaaar.

156 Interestingly, the structures shown in Figure 9 are surprisingly robust to the choice of index level.
157 For any stratospheric (above 100 hPa) index, the resulting anomalies are very similar to the wave-1
158 structure with maximum near 10 hPa in panel a. Conversely, for any tropospheric (below 100
159 hPa) index, the result is very similar to panel b. The pattern cross-correlation between levels of
160 each segment of the atmosphere is greater than 0.9 (Figure A8). The patterns mainly change in
161 amplitude. The tropospheric pattern is maximised by the 300 hPa Asymmetric SAM index and the
162 stratospheric pattern increased monotonically with height.

163 The wave-3 pattern from Figure 7 panel b.2 is very similar to the teleconnection pattern associated
164 with the ENSO. Indeed, Fogt et al. (2011) showed that there is a significant relationship between
165 the SAM and the ENSO. The correlation between the full SAM and the ENSO as measured by the
166 Multivariate ENSO Index (Wolter and Timlin 2011) is -0.19. This relationship is captured entirely

the Asymmetric SAM, as this index has a partial correlation of -0.27 with the MEI, whereas the Symmetric SAM has null partial correlation with the MEI.

c. Impacts

1) TEMPERATURE

Figure 10 shows regression coefficients of each index at 700 hPa with surface temperature for each trimester. It is evident that the Asymmetric and Symmetric SAM indices are associated with overall distinct temperature patterns which can be obscured when using the Full SAM index. The Symmetric SAM signal is weaker than the Asymmetric SAM, as evidenced by the relatively smaller and less statistically significant regression coefficients in row 3 of Figure 10 compared with row 2.

In DJF (column a), the strong negative signal in the tropical Pacific in panel a.1 is mostly associated with the Asymmetric component (panel a.2), as is it largely absent in the Symmetric component (panel a.3). Furthermore, the Asymmetric SAM is also associated with low temperature anomalies in the Indian ocean, but this signal is obscured by the Symmetric variability and thus lost in the Full SAM. Over the continents, the Asymmetric SAM is associated with negative temperature anomalies which, again, mostly disappear in the Full SAM regression.

The patterns seen in MAM and JJA (columns b and c) are not robustly significant in the sense that there are no areas with p-values below 0.05 when controlling for FDR following Wilks (2016). Nevertheless, it is interesting to note that in both trimesters, the sign of the regression is consistently flipped between the Asymmetric and Symmetric regressions. In South America, for example, the Asymmetric SAM is associated with positive temperature anomalies in MAM and negative temperature anomalies in JJA, while the opposite is the case for the Symmetric SAM.

Finally, in SON (column d), there is no significant temperature signal associated with the Symmetric SAM (panel d.3), while the Asymmetric SAM shows a relatively robust signal in the

equatorial Pacific, Australia, and even Southeast South America. This strong signals are reduced in intensity in panel a.3.

2) PRECIPITATION

Regression of the SAM indices with seasonal mean precipitation are shown Figures 11 and 12 for Australia and New Zealand, and South America respectively. (We didn't detect any significant signal in South Africa.)

In Australia (Figure 11), the annual-level regression shows that the Full SAM is associated with a statistically significant increase in precipitation in the Southeastern region (panel a.1), which reproduces the results from Gillett et al. (2006). The separation between Asymmetric and Symmetric SAM suggest that this increase is explained by the Symmetric SAM only in the East coast (panel c.1), which is consistent with the increased easterly flow clearly seen in relation with this index. The Asymmetric SAM appears related to increased precipitation in the West coast of Southeastern Australia (panel b.2), explained by the anomalous *westerly* circulation transporting moist air to the continent.

The seasonal-level regressions show statistically significant anomalies only in SON, with a pattern similar to the annual-level regression (panel a.5). Panels b.5 and c.5 don't show a clear separation between the Asymmetric and Symmetric SAM. If anything, the positive and more significant regression coefficients in panel b.5 vs pane c.5 would suggest more influence of the Asymmetric than the Symmetric SAM, going against the interpretation gathered from the annual-level regressions. This Spring signal is broadly consistent with Hendon et al. (2007), but whereas Hendon et al. (2007) also detected a strong signal in Summer, panel a.2 shows no statistically significant association (although the coefficients have the consistent sign).

212 In South America (Figure 12), the annual-level regression shows that the SAM is associated
213 with statistically significant precipitation decrease in Southeastern South America (SESA) and
214 Southern Chile and non-significant increase in South Brazil, near the South Atlantic Convergence
215 Zone (SACZ) (panel a.1).

216 Panels b.1 and c.1 show a remarkably clean separation between the Asymmetric SAM –associated
217 with the Southeastern South American and Southern Brazilian signals– and the Symmetric SAM
218 –associated with the signal in Southern Chile. This separation is consistent with the mechanisms
219 responsible for these effects. In Southern Chile, the reduced westerly flow reduce moisture transport
220 from the Pacific Ocean (cita?? #FIXME).

221 In Southeastern South America, anomalous meridional winds lead to less precipitation by in-
222 hibiting moisture convergence from the South American Low Level Jet (Silvestri and Vera 2009).
223 The increased precipitation in the South Atlantic Convergence Zone, on the other hand, appears to
224 be related to modulation of the anomalous SAM circulation in SACZ events which lead to more
225 frequent and intense SACZ events during positive SAM (Rosso et al. 2018).

226 There is a small area of increased precipitation with SAM near central Argentina which is
227 also present in the station-based analysis by Gillett et al. (2006) and that is explained by the
228 Asymmetric SAM.

229 Except during Winter, the seasonal-level regression all show these similar patterns although not
230 as cleanly and only in some cases statistically significant.

231 3) SEA ICE

232 Regressions between the Full SAM index and Antarctic Sea Ice Concentrations (Figure 13) show
233 a great deal of variability across seasons. The only statistically significant signal is in Spring, when
234 we observe negative concentraion anomalies in the Northen Weddell Sea (panel a.4) explained

235 by the Asymmetric SAM (panel b.4). Both in Winter and in Spring the Asymmetric SAM is
236 associated with bigger Sea Ice Concentration anomalies in West Antarctica than East Antarctica,
237 with generally decreased concentration East of the Antarctic Peninsula and increased concentration
238 to the West, as expected from the anomalous circulation correlated with this index. The Symmetric
239 SAM signal appears more evenly distributed across the whole ice sheet.

240 *d. Conclusions*

241 We presented a method to systematically separate the zonally asymmetric and zonally symmetric
242 components of the SAM. By itself, the spatial structure and temporal evolution of the SAM
243 shows a strong separation between the stratosphere SAMs. The first EOF in the stratosphere is
244 monopolar in nature while the first EOF in the troposphere is a proper annular mode. Their
245 respective departures from the zonal mean are also different: a zonal wave 1 dominates the
246 stratospheric SAM, waves 3 and 2 dominate the tropospheric SAM. Furthermore, there is little
247 temporal correlation between the tropospheric and stratospheric time series.

248 The zonal asymmetric component of the SAM at each level is even more decoupled between the
249 troposphere and the stratosphere. Their temporal evolution shows essentially zero correlation (Fig-
250 ure 4) and the signal associated with the stratospheric Asymmetric SAM is completely restricted to
251 the stratosphere (Figure 9 panel a). Geopotential height anomalies associated with the tropospheric
252 Asymmetric SAM, on the other hand, do extend to the stratosphere, but those anomalies do not
253 project strongly into the stratospheric Asymmetric SAM.

254 We show that the observed positive trends towards positive SAM is restricted to the tropospheric
255 SAM and is explained by the Symmetric component (Figure \ref{fig:trends}). However, the degree
256 of asymmetry appears to have increased slightly in the last 40 years, as the Asymmetric SAM
257 explains an increasingly proportion of the variance (Figure 6).

In terms of impacts, we see that ..Temperature. . . #FIXME

The patterns of SAM-associated precipitation anomalies are similarly well separated. In South America, we show that negative anomalies observed in Chile related to the SAM are well explained by the Symmetric compomnet, while the precipitation dipole in Southern South America and the South Atlantic Convergence Zone is explained by the Asymmetric component.

1) LIMITATIONS

Our method assumes linearity in the asymmetric component of the SAM. That is, assumes that zonal symmetries associated with positive SAM are oposite and equal to the ones associated with negatie SAM. Fogt et al. (2012)'s composites suggest that this might not be entirely valid, although we argue that much of that apparent non-linearity is due to the heterogenous nature of the selected years for constructing the composites. Using our data (from 1979 to 2018), seasonal composites of zonal anomalies of 700 hPa geopotential height for for SAM+ and SAM- show pattern linear correlations greater than -0.7 for all seasons and are visually very linear (Figure A9). Therefore, we belive that our method is at the very least a reasonable approximation of the phenomenon.

We also asumed that the structure of the SAM zonal anomalies is stable in all seasons. Again, this is not unreasonable, as geopotential zonal anomalies computed by projecting the first EOF of *each season* are very similar to each other (Figure A10).

Silvestri and Vera (2009) showed that impacts linked to the SAM changed rather dramatically before and after 1980. In particular, the negative relationship with precipitation in South America (consistent with Figure 12 panel a.1) was absent in some areas and switched sign in other in the earlier period. The correlation between ENSO and SAM is similarly non-stationary, also disapearing before 1973.

Seeing as both the ENSO-SAM relationship and most of the precipitation impacts in South America are captured by the Asymmetric SAM, the results presented here are most likely period-dependent. Therefore, it is very likely that if we were to repeat this analysis using pre-satellite data, the resulting Asymmetric SAM would look very different.

Acknowledgments. CMAP Precipitation data provided by the NOAA/OAR/ESRL PSL, Boulder, Colorado, USA, from their Web site at <https://psl.noaa.gov/>

NOAA Global Surface Temperature (NOAAGlobalTemp) data provided by the NOAA/OAR/ESRL PSL, Boulder, Colorado, USA, from their Web site at <https://psl.noaa.gov/>

References

Chung, C., and S. Nigam, 1999: Weighting of geophysical data in Principal Component Analysis. *Journal of Geophysical Research: Atmospheres*, **104 (D14)**, 16 925–16 928, doi: 10.1029/1999JD900234.

Fogt, R. L., D. H. Bromwich, and K. M. Hines, 2011: Understanding the SAM influence on the South Pacific ENSO teleconnection. *Clim Dyn*, **36 (7)**, 1555–1576, doi: 10.1007/s00382-010-0905-0.

Fogt, R. L., J. M. Jones, and J. Renwick, 2012: Seasonal Zonal Asymmetries in the Southern Annular Mode and Their Impact on Regional Temperature Anomalies. *J. Climate*, **25 (18)**, 6253–6270, doi:10.1175/JCLI-D-11-00474.1.

Fogt, R. L., and G. J. Marshall, 2020: The Southern Annular Mode: Variability, trends, and climate impacts across the Southern Hemisphere. *WIREs Climate Change*, **11 (4)**, e652, doi: 10.1002/wcc.652.

- 301 Gillett, N. P., T. D. Kell, and P. D. Jones, 2006: Regional climate impacts of the Southern Annular
302 Mode. *Geophysical Research Letters*, **33** (23), doi:10.1029/2006GL027721.
- 303 Hendon, H. H., D. W. J. Thompson, and M. C. Wheeler, 2007: Australian Rainfall and Surface
304 Temperature Variations Associated with the Southern Hemisphere Annular Mode. *J. Climate*,
305 **20** (11), 2452–2467, doi:10.1175/JCLI4134.1.
- 306 Hersbach, H., and Coauthors, 2020: The ERA5 global reanalysis. *Quarterly Journal of the Royal*
307 *Meteorological Society*, **146** (730), 1999–2049, doi:10.1002/qj.3803.
- 308 Osborn, T. J., and P. D. Jones, 2014: The CRUTEM4 land-surface air temperature data set:
309 Construction, previous versions and dissemination via Google Earth. *Earth System Science*
310 *Data*, **6** (1), 61–68, doi:10.5194/essd-6-61-2014.
- 311 Raphael, M. N., 2004: A zonal wave 3 index for the Southern Hemisphere. *Geophysical Research*
312 *Letters*, **31** (23), doi:10.1029/2004GL020365.
- 313 Rosso, F. V., N. T. Boiaski, S. E. T. Ferraz, and T. C. Robles, 2018: Influence of the Antarctic
314 Oscillation on the South Atlantic Convergence Zone. *Atmosphere*, **9** (11), 431, doi:10.3390/
315 atmos9110431.
- 316 Silvestri, G., and C. Vera, 2009: Nonstationary Impacts of the Southern Annular Mode on Southern
317 Hemisphere Climate. *J. Climate*, **22** (22), 6142–6148, doi:10.1175/2009JCLI3036.1.
- 318 Smith, T. M., R. W. Reynolds, T. C. Peterson, and J. Lawrimore, 2008: Improvements to NOAA’s
319 Historical Merged Land–Ocean Surface Temperature Analysis (1880–2006). *J. Climate*, **21** (10),
320 2283–2296, doi:10.1175/2007JCLI2100.1.
- 321 Vose, R. S., and Coauthors, 2012: NOAA’s Merged Land–Ocean Surface Temperature Analysis.
322 *Bull. Amer. Meteor. Soc.*, **93** (11), 1677–1685, doi:10.1175/BAMS-D-11-00241.1.

- 323 Wilks, D. S., 2016: “The Stippling Shows Statistically Significant Grid Points”: How Research
324 Results are Routinely Overstated and Overinterpreted, and What to Do about It. *Bull. Amer.*
325 *Meteor. Soc.*, **97** (12), 2263–2273, doi:10.1175/BAMS-D-15-00267.1.
- 326 Wolter, K., and M. S. Timlin, 2011: El Niño/Southern Oscillation behaviour since 1871 as diag-
327 nosed in an extended multivariate ENSO index (MEI.ext). *International Journal of Climatology*,
328 **31** (7), 1074–1087, doi:10.1002/joc.2336.
- 329 Xie, P., and P. A. Arkin, 1997: Global Precipitation: A 17-Year Monthly Analysis Based on
330 Gauge Observations, Satellite Estimates, and Numerical Model Outputs. *Bull. Amer. Meteor.*
331 *Soc.*, **78** (11), 2539–2558, doi:10.1175/1520-0477(1997)078<2539:GPAYMA>2.0.CO;2.

APPENDIX

Extra figures

334	LIST OF FIGURES	
335	Fig. 1. Spatial patterns of the first EOF of 700 hPa geopotential height	20
336	Fig. 2. Time series for the asymmetric SAM and symmetric SAM and density estimates	21
337	Fig. 3. Correlation between the Symmetric and Asymmetric SAM at each level for lag zero and lag	
338	-1 (Asymmetric leads Symmetric)	22
339	Fig. 4. Cross correlation between levels of the Full, Asymmetric and Symmetric SAM	23
340	Fig. 5. Decadal normalised trends for each index at each level for annual (row a) and seasonal values	
341	(rows b-e) for the period 1979-2018	24
342	Fig. 6. Decadal trends for explained variance of each index at each level for the period 1979-2018 . . .	25
343	Fig. 7. Regression patterns of geopotential height at 30, 300 and 700 hPa with the Full, Asymmetric	
344	and Symmetric SAM	26
345	Fig. 8. Planteray wave amplitude for the regression patterns at 50 and 700 hPa	27
346	Fig. 9. Asymmetric coefficient of the multiple regression of mean monthly geopotential height	
347	anomalies between 65 and 40 South	28
348	Fig. 10. Regression pattern of surface temperature with Asymmetric and Symmetric SAM	29
349	Fig. 11. Same but for oceania	30
350	Fig. 12. Same but for america	31
351	Fig. 13. Seasonal regression of SAM indices with sea ice concentration	32
352	Fig. A1. Lag-correlation between Symmetric and Asymmetric SAM at each level.	33
353	Fig. 14. Cross-correlation functions for each index and two differnet base levels	34
354	Fig. A3. Fourier spectrum of each timeseries. The shading indicates de 95% area derived by fitting	
355	an AR process to each series and bootstrapping 5000 simulated samples.	35
356	Fig. A4. Autocorrelation functions of each timeseries	36
357	Fig. A8. Pattern cross-correlation #FIXME!	37
358	Fig. 15. 700 hPa Geopotetnial height zonal anomalies of composites of positive and negative SAM	
359	months selected using 1 standard deviation as threshold	38
360	Fig. 16. Zonal of projection of 700 hPa onto the first EOF of each season	39

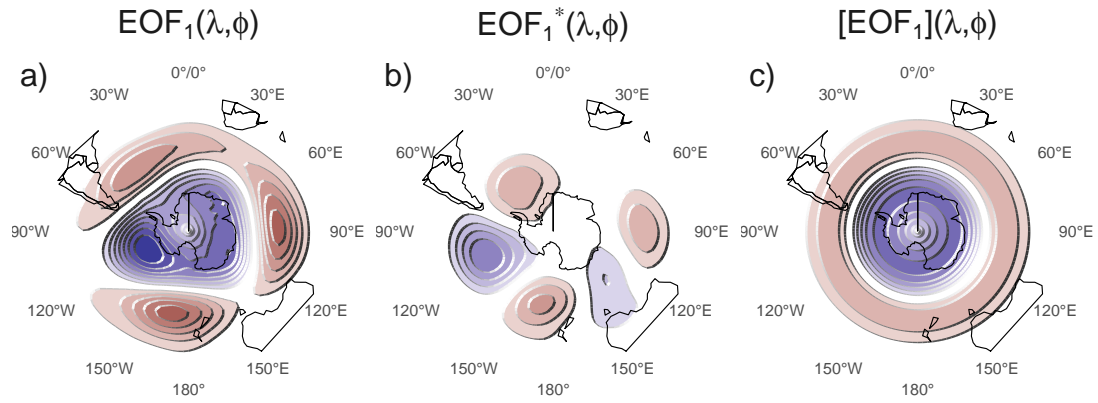


FIG. 1: Spatial patterns of the first EOF of 700 hPa geopotential height. Full field (left), zonally asymmetric component (middle) and zonally symmetric component (right). Arbitrary units.

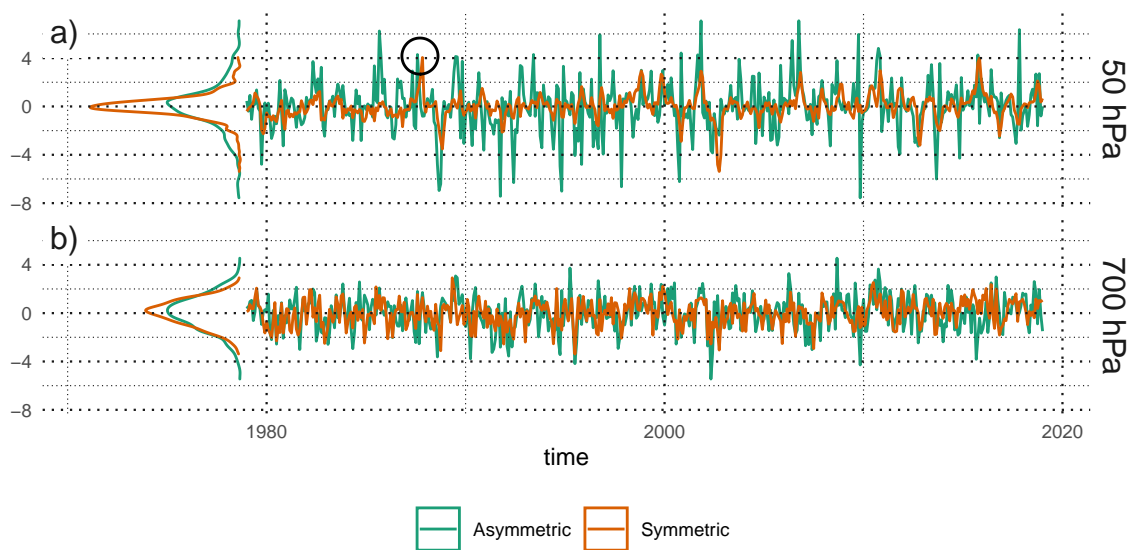


FIG. 2: Time series for the asymmetric SAM and symmetric SAM and density estimates.

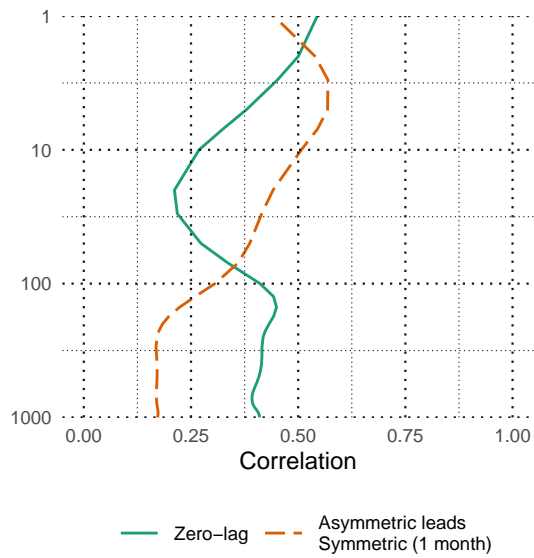


FIG. 3: Correlation between the Symmetric and Asymmetric SAM at each level for lag zero and lag -1 (Asymmetric leads Symmetric).

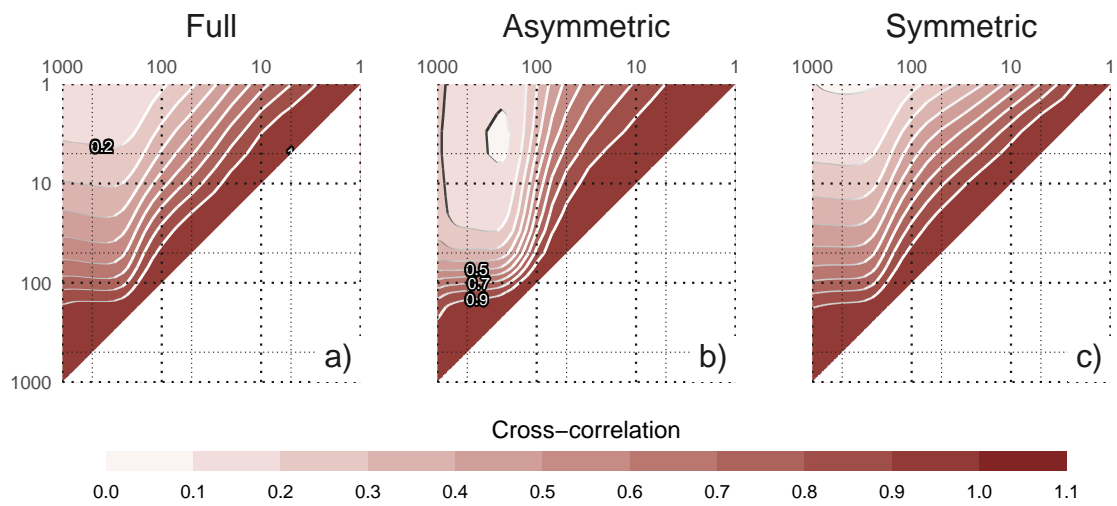


FIG. 4: Cross correlation between levels of the Full, Asymmetric and Symmetric SAM.

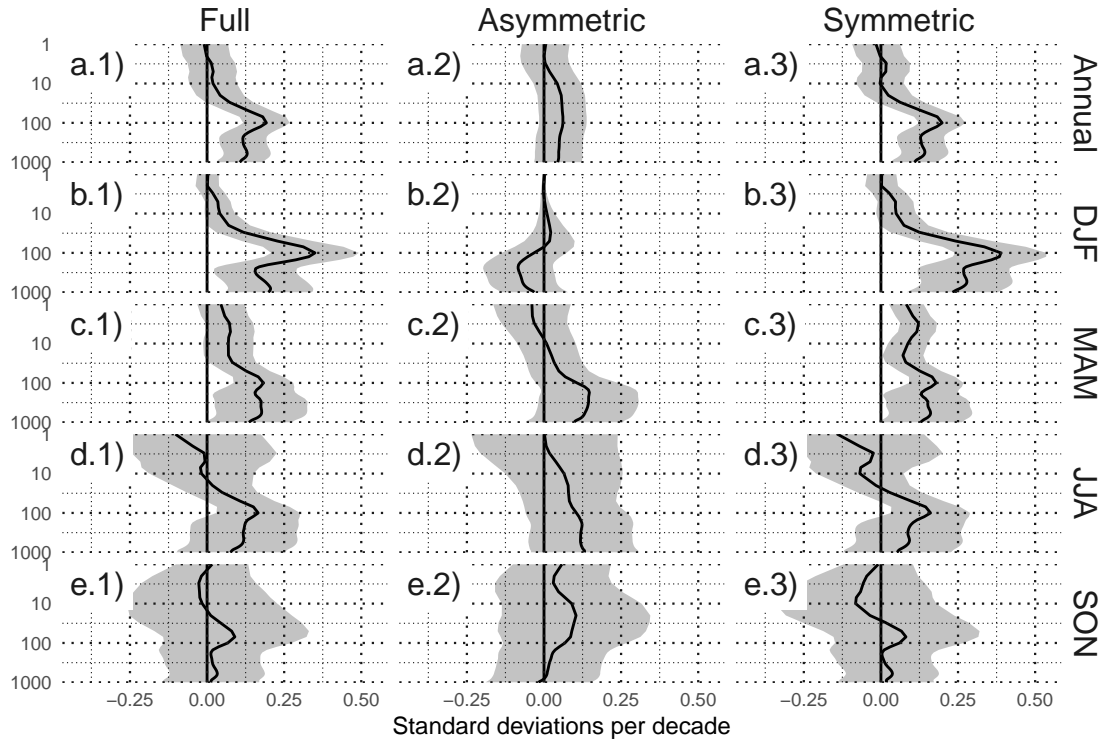


FIG. 5: Decadal normalised trends for each index at each level for annual (row a) and seasonal values (rows b-e) for the period 1979-2018. Shading indicates the 95% confidence interval.

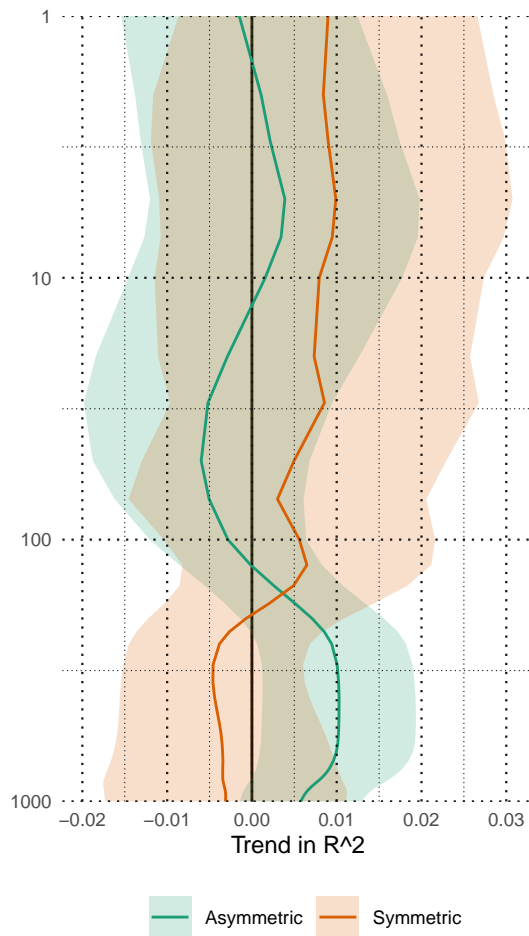


FIG. 6: Decadal trends for explained variance of each index at each level for the period 1979-2018. Shading indicates the 95% confidence interval.

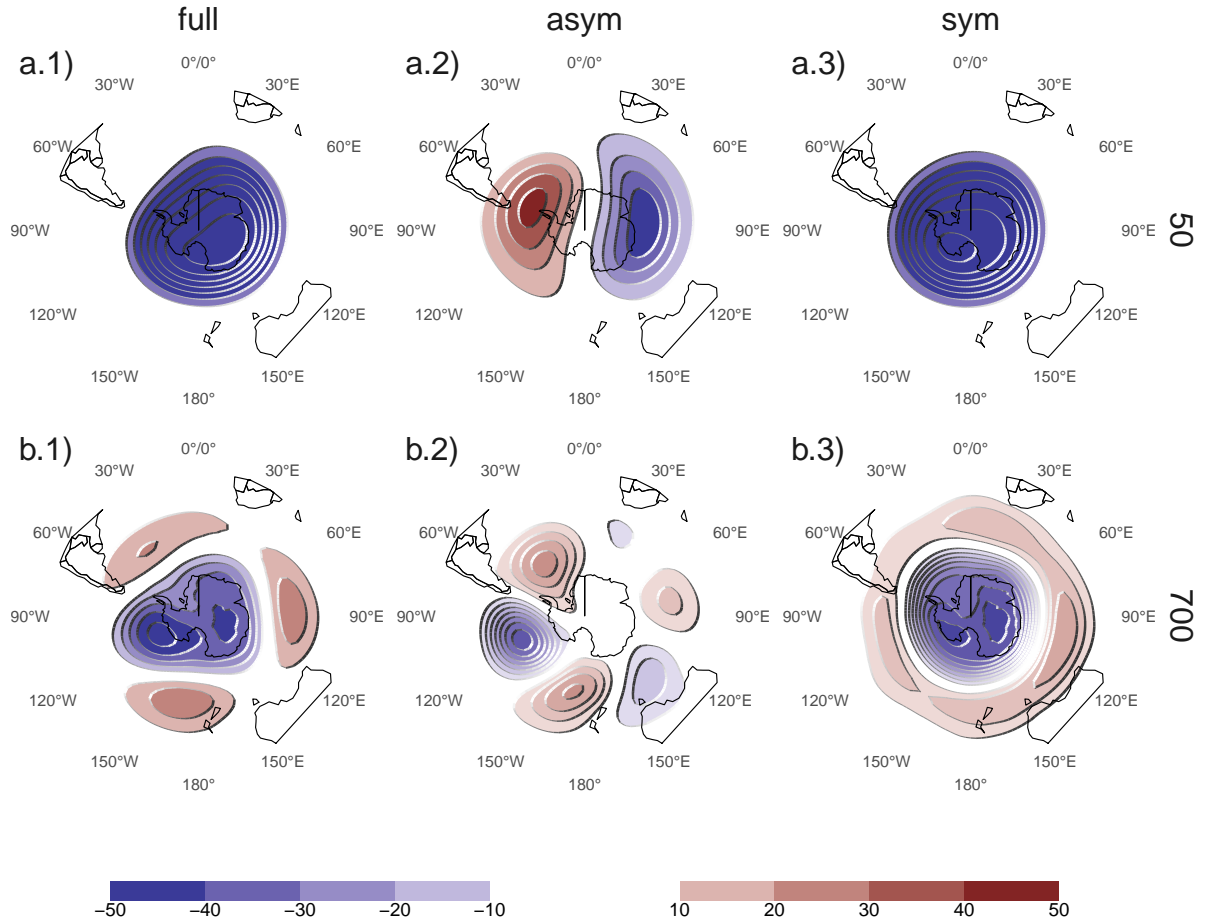


FIG. 7: Regression patterns of geopotential height at 30, 300 and 700 hPa with the Full, Asymmetric and Symmetric SAM. The regression patterns for Asymmetric and Symmetric SAM are the result of one multiple regression using both indices, not of two simple regressions involving each index by itself.

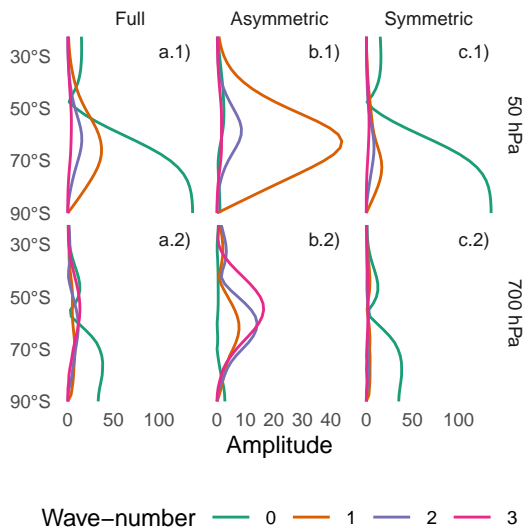


FIG. 8: Planetary wave amplitude for the regression patterns at 50 and 700 hPa. Note the varying x axis.

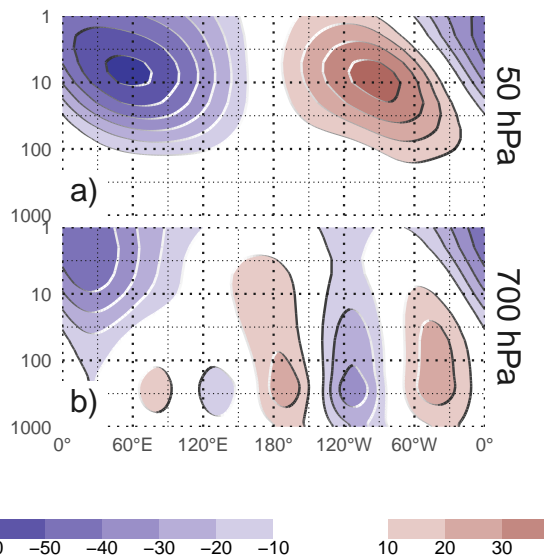


FIG. 9: Asymmetric coefficient of the multiple regression of mean monthly geopotential height anomalies between 65 and 40 South. (#FIXME this caption needs some love)

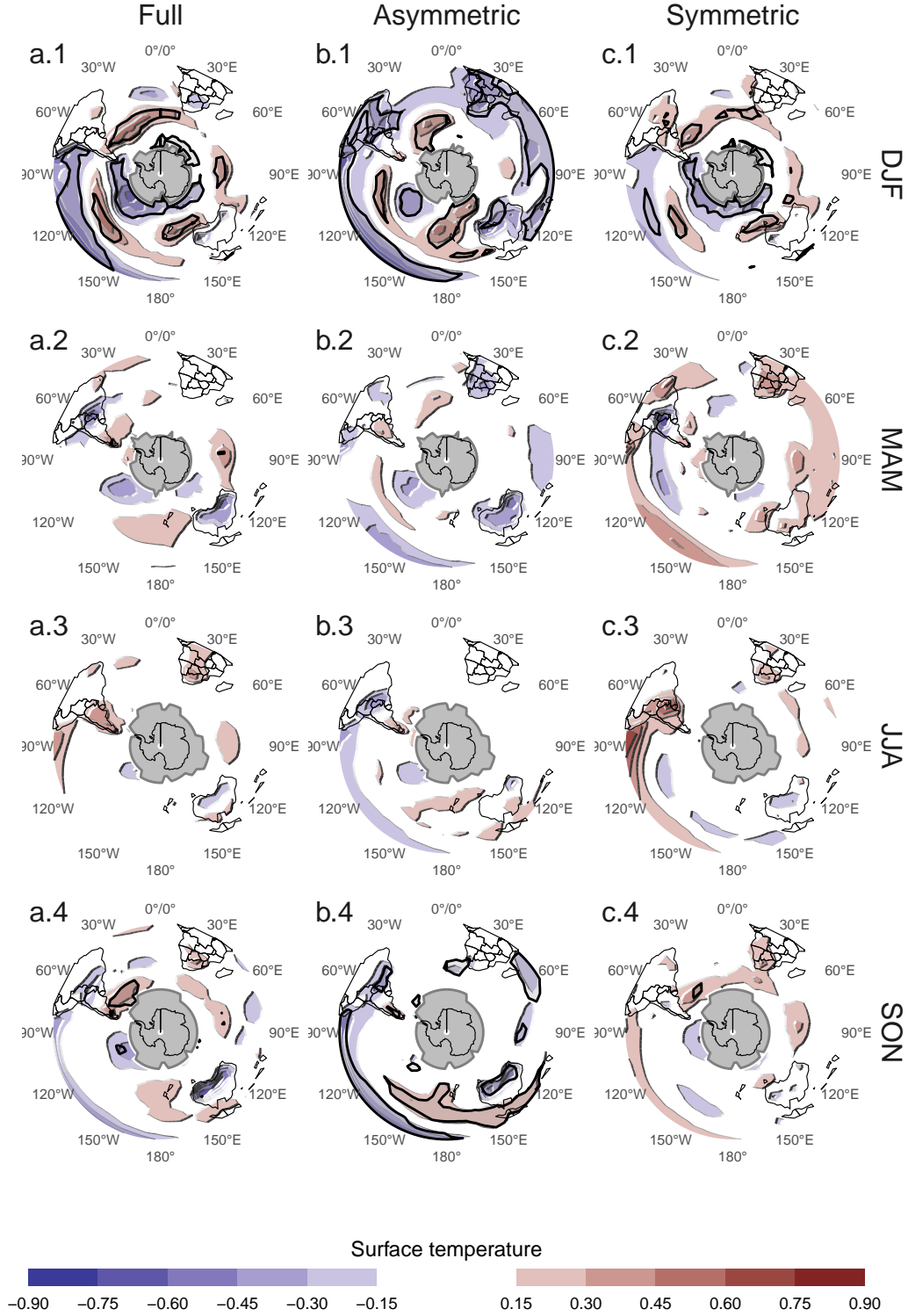


FIG. 10: Regression pattern of surface temperature with Asymmetric and Symmetric SAM. P-values smaller than 0.05 (controlling for False Detection Rate) as hatched areas. Gray areas have more than 15% of missing data.

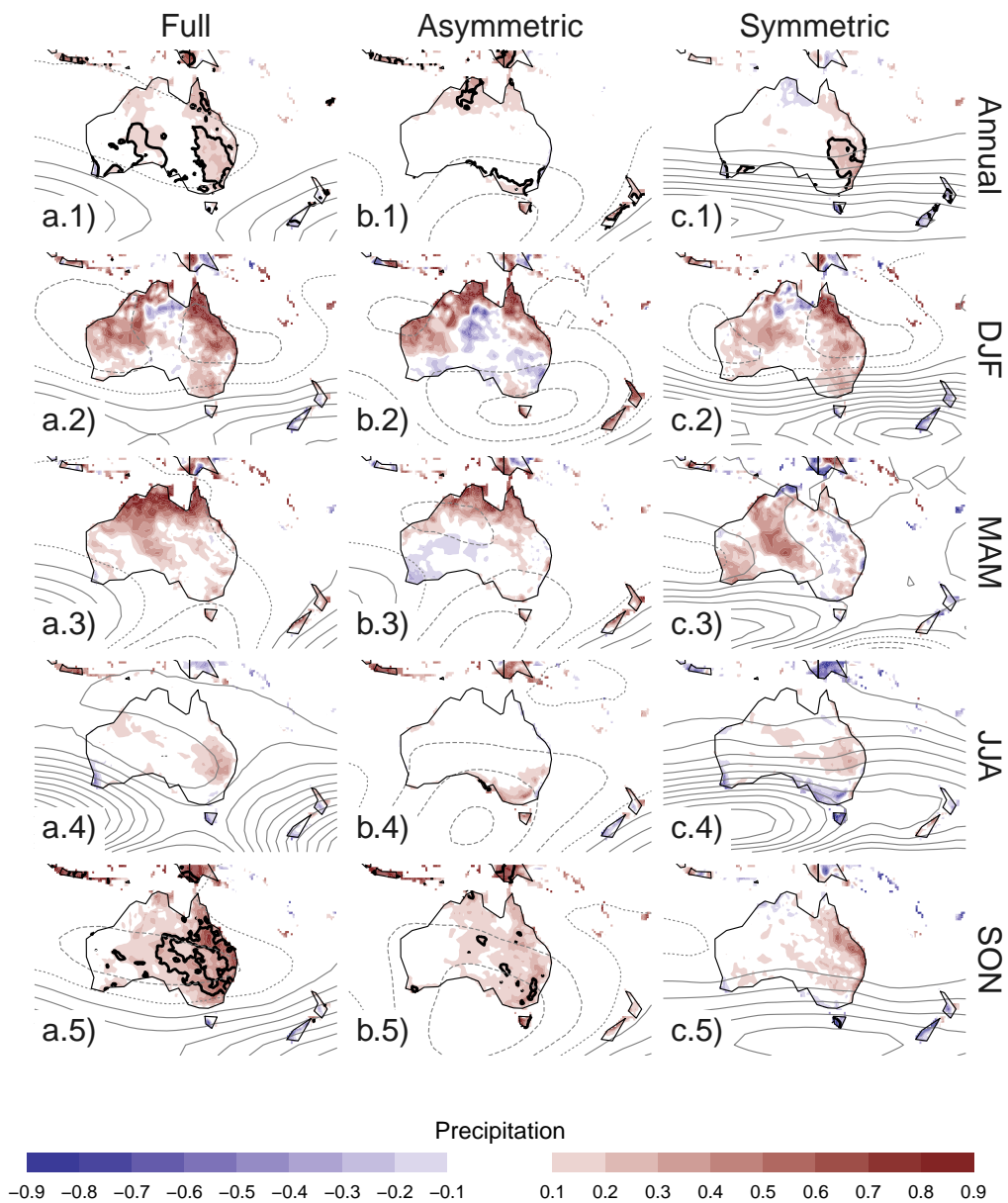


FIG. 11: Same but for oceania

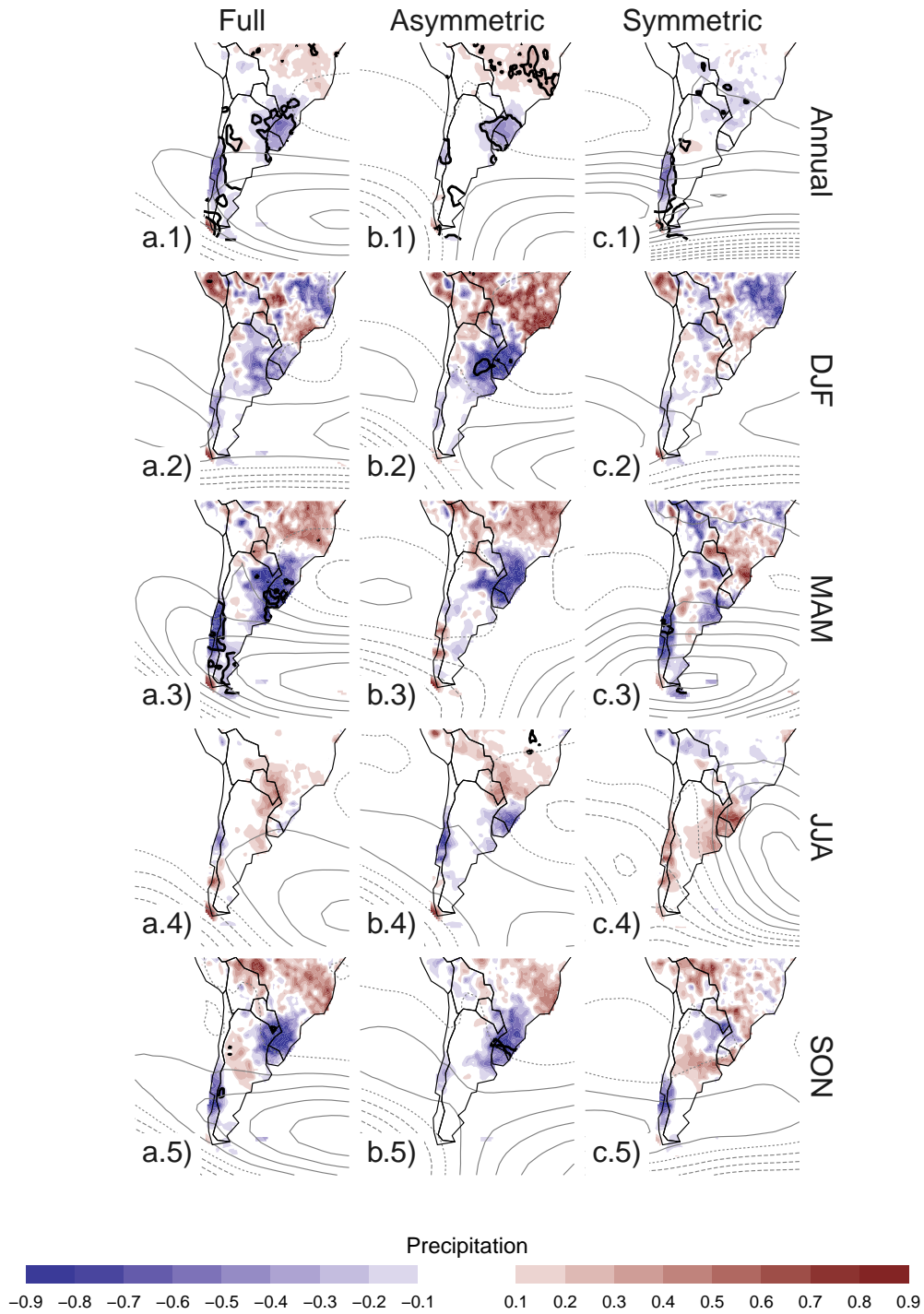


FIG. 12: Same but for america

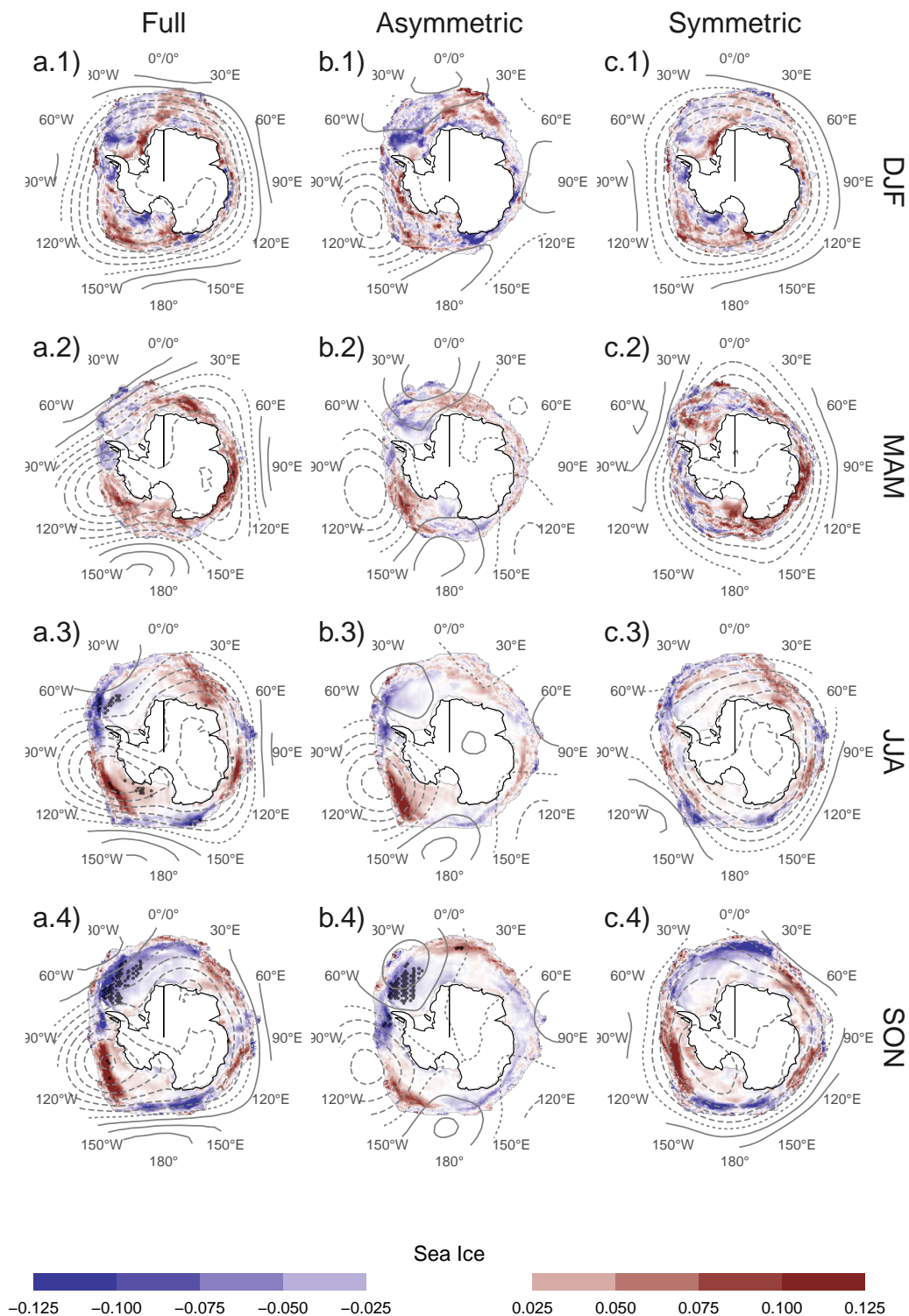


FIG. 13: Seasonal regression of SAM indices with sea ice concentration. #FIXME

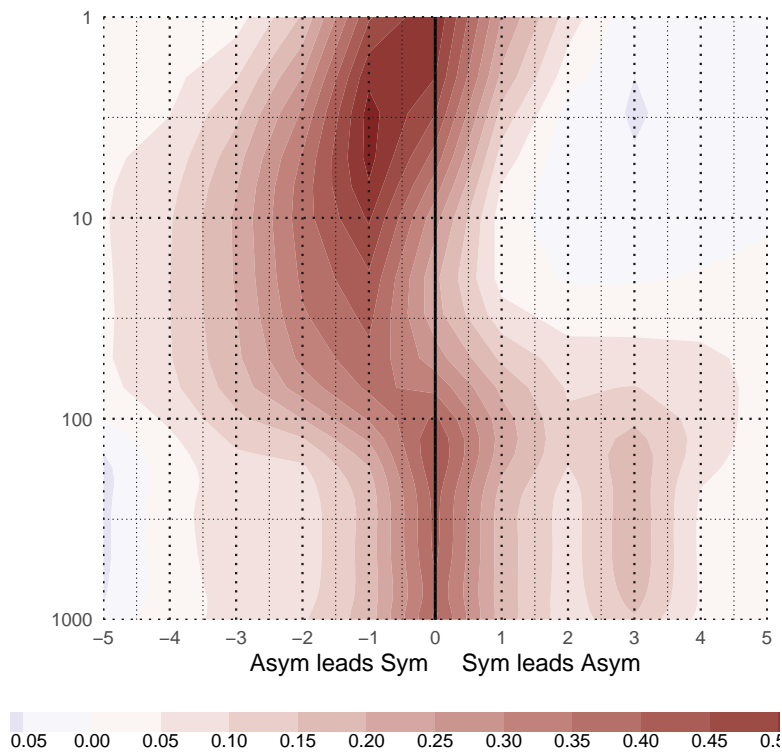


Fig. A1: Lag-correlation between Symmetric and Asymmetric SAM at each level.

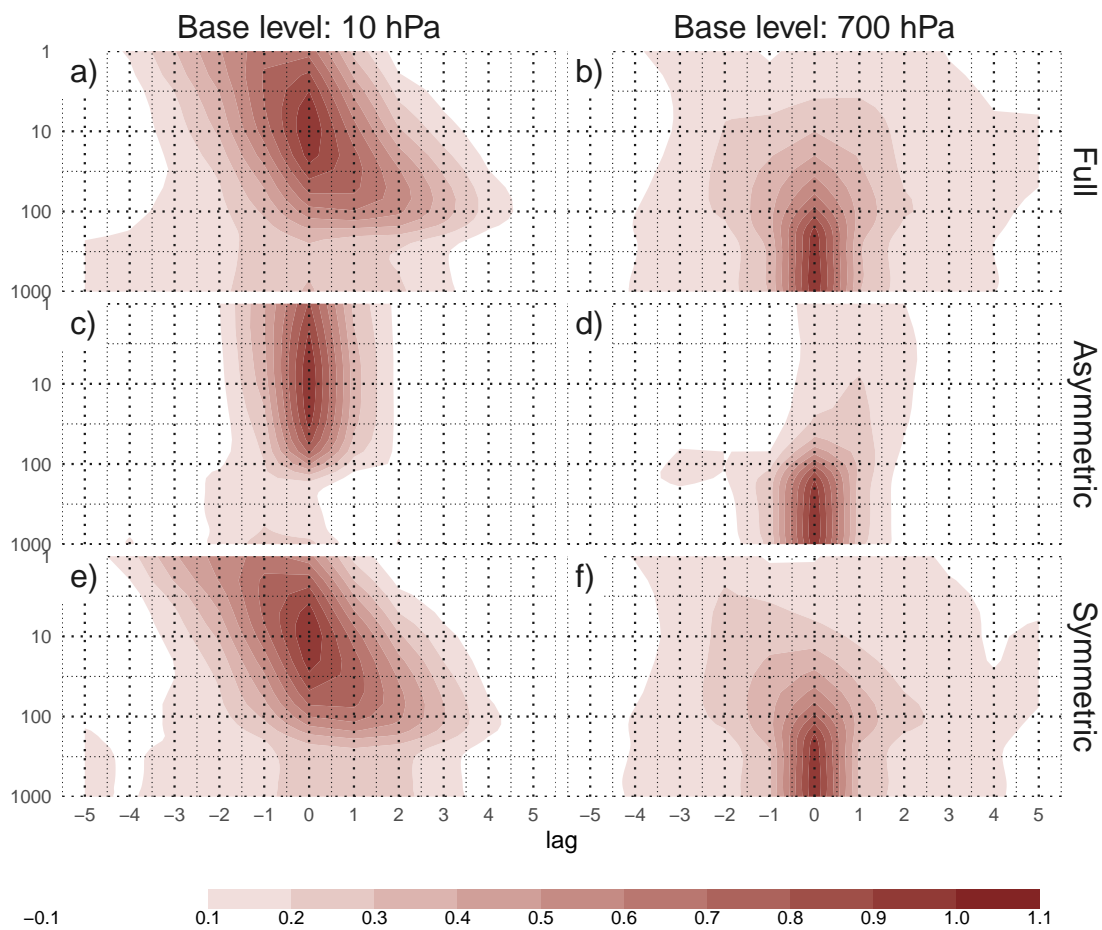


FIG. 14: Cross-correlation functions for each index and two different base levels.

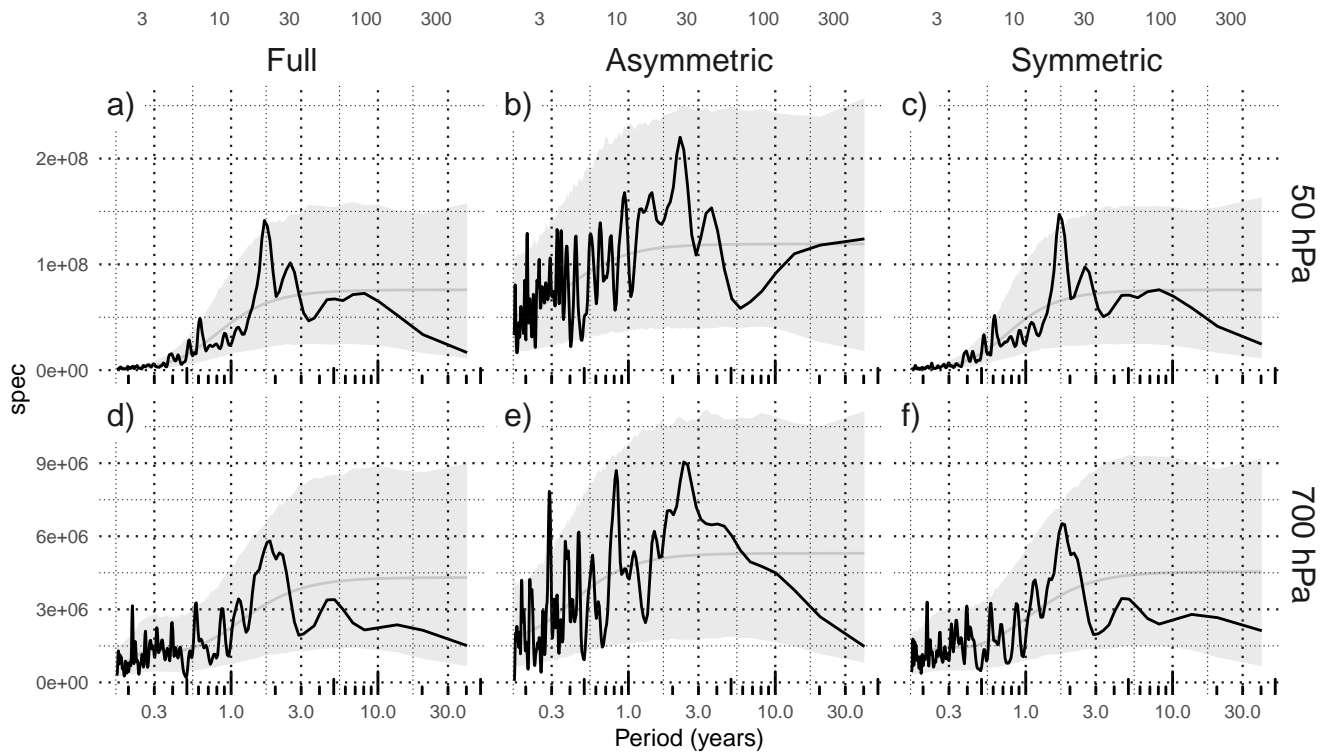


Fig. A3: Fourier spectrum of each timeseries. The shading indicates the 95% area derived by fitting an AR process to each series and bootstrapping 5000 simulated samples.

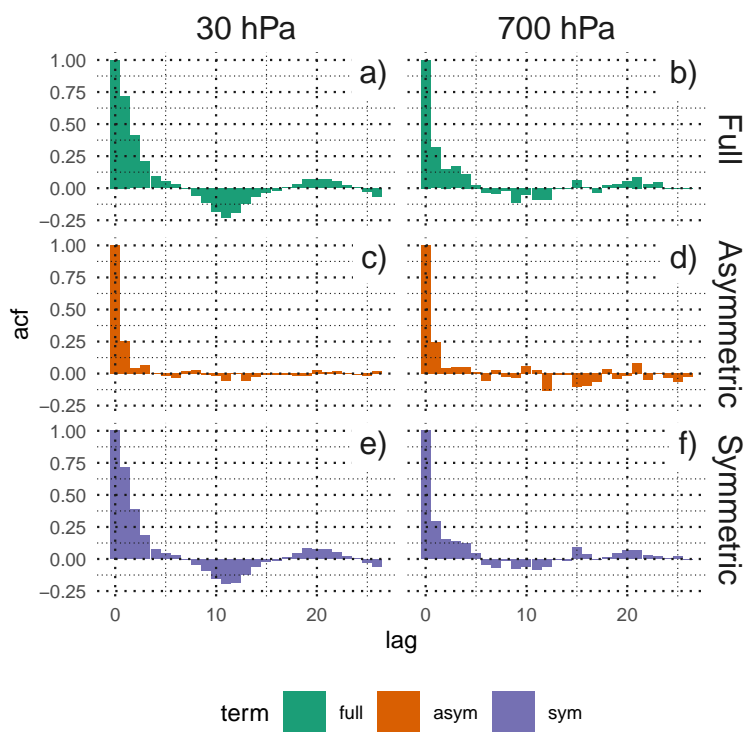


Fig. A4: Autocorrelation functions of each timeseries

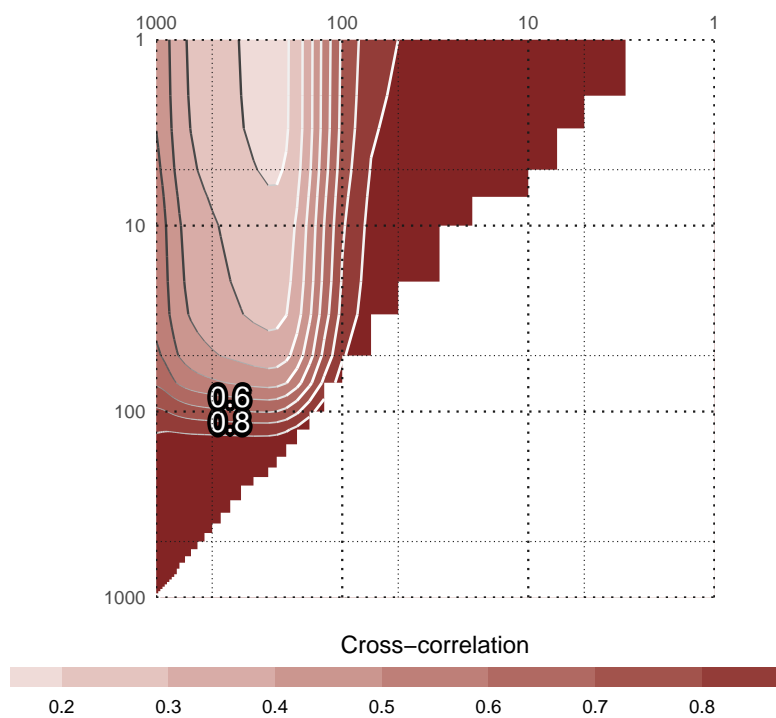


Fig. A8: Pattern cross-correlation #FIXME!

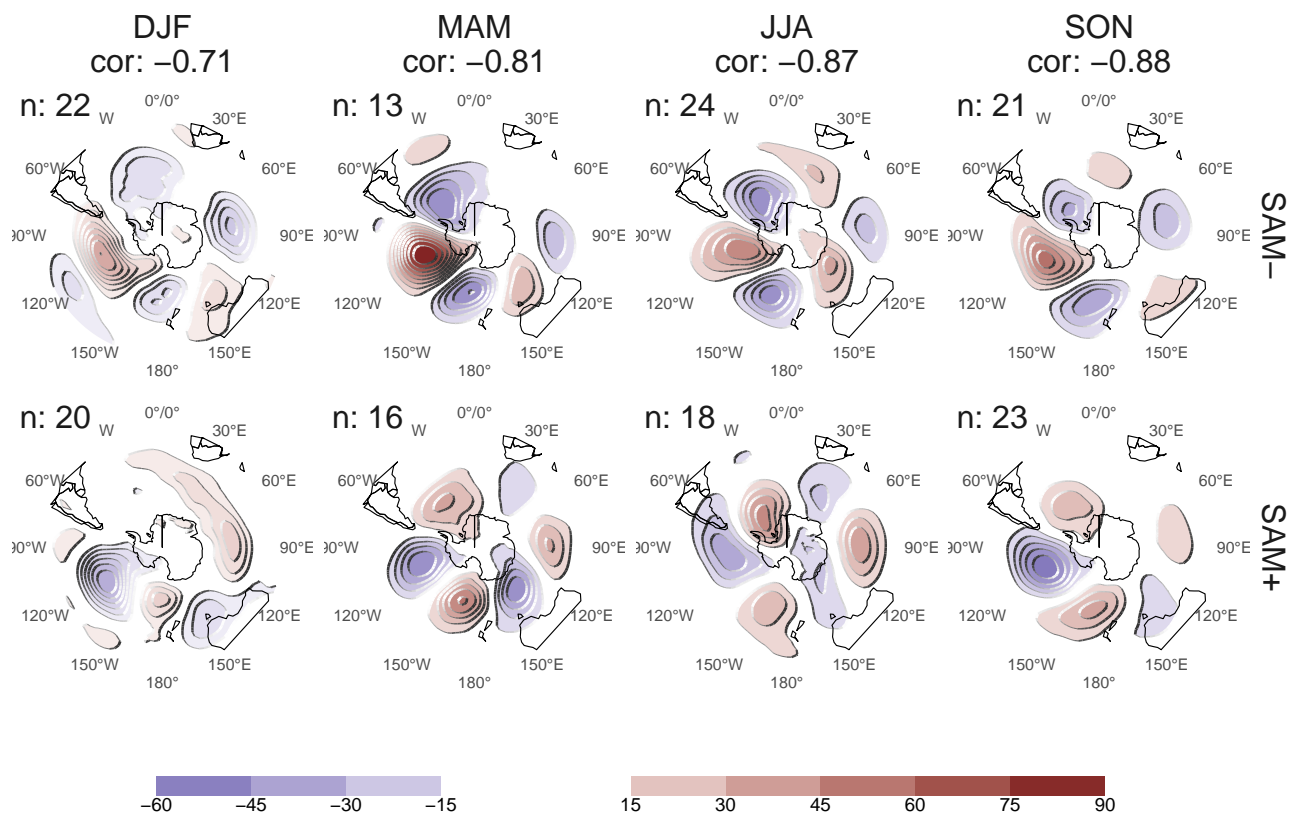


FIG. 15: 700 hPa Geopotential height zonal anomalies of composites of positive and negative SAM months selected using 1 standard deviation as threshold. Numbers in the column headers are pattern correlation between SAM+ and SAM- composites and number of monthly fields used to construct the composites.

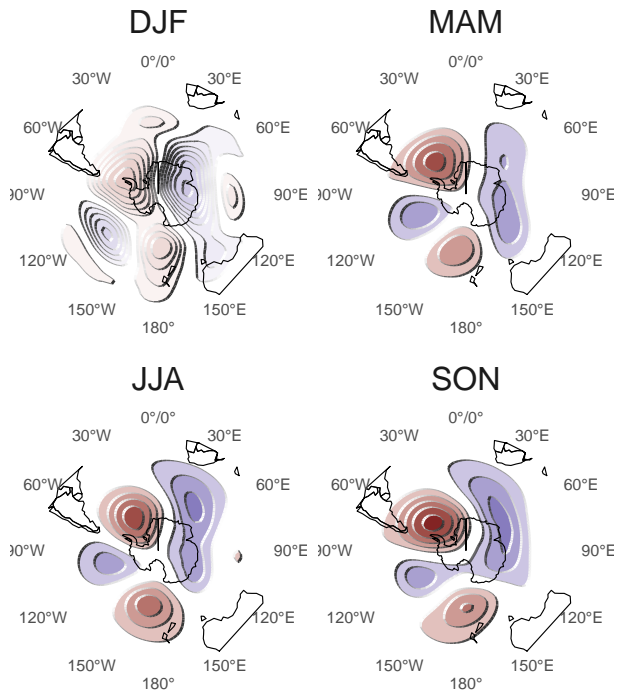


FIG. 16: Zonal of projection of 700 hPa onto the first EOF of each season.